Surface Defect Detection and Identification of Hot Rolled Strip Steel Based on Combined Feature Extraction and Probabilistic Neural Network

Chang Cai, Junsheng Wang*, Jiawei Liu, Hongmei Zhang, Lei Song

Abstract—**In the rolling process of hot-rolled strip steel, variations in mill operating conditions and process parameters may induce multiple surface defects on the produced strip steel. Product quality is seriously affected by strip defects, which have apparent similarities, and defect detection leads to poor accuracy. This study proposes a hybrid feature fusion approach integrated with a probabilistic neural network (PNN) to enhance computational efficiency and recognition accuracy in hot-rolled strip steel surface defect detection. Firstly, a comprehensive image processing method and an improved Multi-Scale Retinex (MSR) algorithm are used to construct a defect recognition system and process image enhancement. The block adaptive threshold method quickly identifies the suspected defect target in the enhanced image, allowing for precise location and segmentation of the defect area. The gray co-occurrence matrix and maximum entropy method are adopted, and the combined features are extracted from the defect region as the classification and discrimination parameters. Defects are classified by Logistic particle swarm optimization-based probabilistic neural network (LPSO-PNN). The existing classification algorithm and experimental results are verified. The verification results show that hot-rolled strip steel surface defects are extracted based on combination features, then a probabilistic neural network has been employed for detection and recognition, and the accuracy rate reached 99.57%.**

Index Terms—**improved MSR algorithm, combination features, probabilistic neural network, strip steel defect detection, particle swarm optimization.**

I. Introduction

IN the complex hot rolled strip steel production process, affected by equipment and technological conditions, there are inevitably different kinds of defects on the strip surface.

Based on causative factors and morphological characteristics, surface defects in steel plates are primarily categorized into five defects: scratches, inclusions, patches, scabs, and surface pits. These imperfections pose significant challenges for manual detection due to their dimensional variability combined with visually indistinct features or undetectable attributes [1][2][3][4]. As surface defects not only significantly compromise the steel's structural integrity but also detrimentally affect its fatigue resistance and wear characteristics [5][6], computer vision-based detection systems [7][8][9] have been developed to address these critical quality issues. These advanced systems employ a multi-stage analytical approach involving image enhancement [10], precise segmentation, and discriminative feature extraction, enabling reliable defect identification and classification that effectively mitigates quality risks in strip steel production.

Computer vision-based detection systems remain susceptible to performance degradation caused by non-uniform illumination in industrial environments. Even with stringently controlled lighting conditions, persistent interference persists due to the intrinsic limitations of ambient light modulation in steel surface inspection. Current preprocessing methodologies can partially mitigate these photometric distortions, thereby enhancing image fidelity. Advanced computational enhancement techniques enable amplification of inter-class feature discriminability, suppression of non-essential image components, and optimization of signal-to-noise ratio. This tripartite approach not only elevates the information entropy of visual data but also significantly reduces misclassification rates in downstream defect detection and categorization processes [11]. The conventional multi-scale retinex (MSR) algorithm employs multi-scale filtering operations to compute reflectance components for image enhancement. However, its manual weight assignment mechanism introduces operator-dependent bias that compromises algorithmic consistency. To address this limitation, we propose an entropy-optimized adaptive MSR algorithm that automatically determines optimal weighting coefficients through quantitative analysis of information entropy distribution across scale spaces. This innovation establishes a robust preprocessing foundation for subsequent defect image segmentation and discriminative feature extraction [12].

Manuscript received December 10, 2024; revised May 16, 2025.

This work was supported by the National Key Research and Development Program: Research on Cloud Manufacturing Collaborative Platform for Value Chain Network (2022YFE0197600).

Chang Cai is a doctoral student of School of Electronic and Information Engineering, University of Science and Technology Liaoning, Anshan, Liaoning, 114051, China (e-mail: caichang_cc@163.com).

Junsheng Wang is a professor of Beijing Research Institute of Ansteel Group Co., Ltd., Beijing 100010, China (Corresponding author, e-mail: phdwjs@163.com).

Jiawei Liu is a senior engineer of Ansteel Group Automation Co., Ltd., Anshan 114000, China (e-mail: liujiawei1975@163.com).

Hongmei Zhang is a professor of School of Materials and Metallurgy, University of Science and Technology Liaoning, Anshan 114000, China (e-mail: zhanghm@ustl.edu.cn).

Lei Song is an associate professor of School of Electronic and Information Engineering, University of Science and Technology Liaoning, Anshan 114000, China (e-mail: 2327603962@qq.com).

In contrast to traditional edge detection methods, the dynamic threshold segmentation approach [13] demonstrates superior performance in identifying irregularly shaped defects within preprocessed industrial images. While the local adaptive threshold method demonstrates superior segmentation performance under complex illumination by utilizing grayscale statistical features (including mean intensity, median value, standard deviation, and interquartile range) within pixel neighborhoods to determine dynamic thresholds, it presents three principal limitations high computational complexity, slow processing speed, and sensitivity to parameter selection [14]. Addressing these constraints, Truong and Kim [15] developed an entropy-weighted Otsu segmentation framework that autonomously detects micro-defect regions through entropy-based probability distribution optimization, significantly improving detection accuracy.

This study proposes a novel block adaptive thresholding with a singularity density analysis framework that achieves rapid identification of potential defect targets through localized threshold adaptation. The proposed methodology enables enhanced segmentation precision through multi-scale singularity quantification and optimized defect boundary delineation via adaptive block-wise parameter optimization. Furthermore, the developed system addresses the critical challenge in steel surface inspection, efficient extraction, and reliable classification of defect signatures from high-volume industrial image datasets. Following defect segmentation, our methodology employs a dual-feature extraction approach that integrates morphological characteristics with textural patterns for comprehensive defect classification. The feature engineering process comprises two principal components: (1) textural quantification through gray-level co-occurrence matrix (GLCM) analyses [16][17], extracting five discriminative parameters: energy (En), contrast (Co), correlation (Cl), entropy (Et), and inverse difference moment (Idm) [18]; (2) morphological characterization involving geometric descriptors derived from maximum-entropy threshold segmentation [19], including area ratio (Ar) and aspect ratio (As), and the extracted combined features were classified by deep learning technology.

The remarkable progress in computational capabilities [20] coupled with the curation of large-scale industrial datasets has driven transformative advancements in deep learning-based classification systems, achieving unprecedented performance benchmarks [21][22]. Demonstrating this technological evolution, Liu et al. [23] implemented a probabilistic neural network (PNN) architecture for multi-scale entropy feature extraction from biological tissue ultrasonic echo signals. Their comparative analysis revealed two distinct advantages of PNN over conventional methods: accelerated training convergence and superior recognition accuracy. Crucially, the classification fidelity of PNN models exhibits strong dependence on the smoothing factor parameter σ, a critical hyperparameter governing probability density estimation that requires careful calibration through optimization techniques [24].

However, conventional particle swarm optimization (PSO) algorithms exhibit three fundamental limitations: suboptimal convergence rates, solution instability, and premature convergence to local optima, which collectively compromise defect recognition accuracy [25][26]. To address these critical challenges, we propose an enhanced PSO framework that integrates adaptive inertia weight and dynamic neighborhood strategies.

This study develops an optimized (MSR) framework integrating multi-scale guided filtering and adaptive weight allocation, which achieves enhanced image quality while significantly improving machine vision system robustness under varying illumination scenarios. Then, the BAT-SDA method is used to quickly identify the suspected defect target. The images with defects are selected from the mass surface images of hot-rolled strip, and the suspected defect area is clipped. The grey scale covariance matrix and maximum entropy value method extracted the defective region's texture features and shape features. The extracted feature combination served as discriminative parameters and was subsequently fed into the LPSO-PNN defect classification model. The particle swarm was updated and optimized by using a nonlinear decreasing inertia weight coefficient and a Logistic chaotic map. The global particle traversal optimization capability is strengthened. Finally, the steel surface defect category is outputted by PNN. The proposed methodology significantly enhances defect detection accuracy, demonstrating industrial applicability for automated strip surface inspection systems.

II. Defect Image Processing and Feature Extraction

In this study, a strip surface defect inspection system was established for the hot-rolled 2150 production line. The system configuration utilizes a vertically mounted WP-UT030 CCD industrial camera positioned perpendicular to the steel plate surface, complemented by an overhead coaxial illumination unit. Coaxial light source WP-CO250260 is used as the external light source with 33W power. It is suitable for the detection of five types of defects on the strip steel surface.

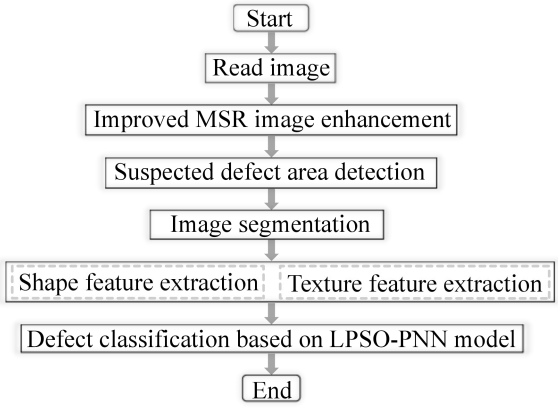

Fig. 1. Strip steel surface defect classification process

Fig. 1 demonstrates the MSR algorithm to enhance the defective features in the captured steel bar image, then the suspected defect area of the image is detected, the image is segmented, the image correlation, contrast, energy, entropy, inverse different moment and other parameters of the image are extracted, and the Ar, As and roundness (Ro) of the target are extracted. Texture and shape features demonstrating strong discriminative power were designated as classification parameters. Finally, the LPSO-PNN classification model was built, six features of Co, En, Idm, Ar, As, and Ro were input,

and the defects on the steel surface were output.

A. Image Enhancement Processing

In high-speed hot-rolled strip steel production environments with variable illumination, maintaining stable image quality is challenging. However, applying advanced image preprocessing techniques can effectively mitigate the impact of ambient illumination on visual data acquisition. When dealing with images, traditional MSR algorithms [27][28] will lose the image structure information and damage the image edges. Therefore, we adopted the multi-scale guide filtering and adaptive weighting. We employed guided filtering in place of Gaussian filtering, and subsequently used image information entropy features to automatically determine the adaptive weight. Specific values were assigned based on information entropy, adapting to variations across different images. The process is detailed below.

We set guided filters of different scales as the center-surround function, used the input image as the guided image, and calculated the retinex enhancement results of different scales:

$$R_n^{\wedge}(x,y) = lg[S_n(x,y)] - lg[g_n(x,y)^{*}S_n(x,y)] \quad (1)$$

* is the convolution, n is the scale, $S_n(x,y)$ is the original image, $g_n(x,y)$ is the guided filter, and $g_n(x,y)^{*}S_n(x,y)$ is the illumination component.

The spatial characteristics of grayscale distribution are represented by the neighborhood mean value within the image. The ratio of the feature binary group (i,j) is composed of it and the gray value of an image pixel:

$$P_{ij} = \frac{N(i,j)}{M} \quad (2)$$

$N(i,j)$ is the frequency. (i,j) denotes pixel intensity and the neighborhood mean intensity (0≤i, j≤255), and M is the total pixel count of the image.

The spatial entropy of a discrete image is defined as:

$$H = -\sum_{i=0}^{255}\sum_{j=0}^{255} P_{ij}\, logP_{ij} \quad (3)$$

The weight calculation formula of each scale image:

$$W_k = \frac{H_k}{\sum_{l=1}^{K} H_l} \quad (4)$$

H_k is the 2D information entropy and k denotes scale total. The enhancement results of different scales were weighted and averaged:

$$R^{\wedge}(x,y) = \sum_{n=1}^{N} w_k\, R_n^{\wedge}(x,y) \quad (5)$$

The reflected component $R\,(x,y)$is obtained by quantizing $R^{\wedge}(x,y)$:

$$R\,(x,y) = exp(R_n^{\wedge}(x,y)) \quad (6)$$

Fig. 2(a) and (b) show the types of defects for scratches and inclusions, respectively. As can be seen from the comparison, Fig. 2(b) shows the edge of the target more clearly than Fig. 2(a), reduces the interference of the background image, effectively improves the quality of the image.

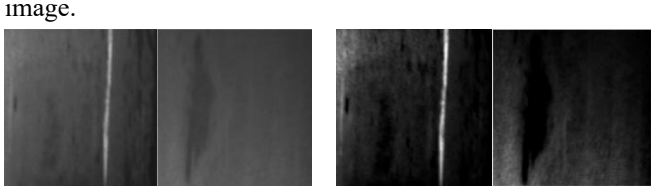

(a)Original image (b)Improved MSR enhanced images

Fig. 2. Comparison before and after improved MSR algorithm

B. Suspected defect area detection

Steel strip surface inspection on real-time defect extraction and classification from high-throughput imaging data. The threshold segmentation method [29] can be used when there are obvious differences in the defect images, but the effect is not ideal under the condition of unstable shading and illumination, and the adaptive threshold segmentation method can solve these problems well. The proposed method detects the suspected defective regions of the original image, improves the efficiency of the system's analysis, and reduces the amount of data transmission. The process of detection is as follows:

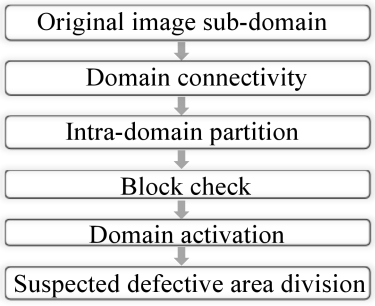

Fig. 3. Defect area detection process

Firstly, we defined the extended side length subdomain according to the image size, carried out the original image subdomain, and then carried out the intra-domain segmentation according to the fixed template. According to the grayscale, color difference, and distribution characteristics, a fast block test is carried out to activate the domain with an active block, and the finite domain connectivity is carried out according to the domain's connectivity. Finally, the domain information is encapsulated, and the image is segmented.

Our defect detection framework synergizes adaptive block thresholding with singularity density profiling, enabling rapid anomaly identification followed by precision segmentation. The flow chart is as follows:

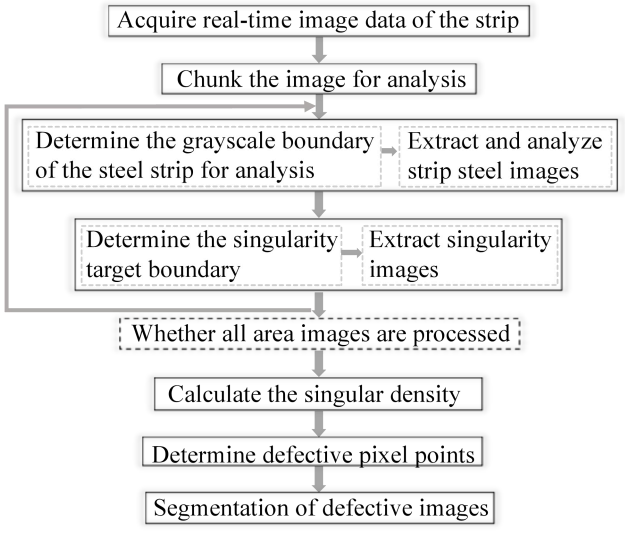

Fig. 4. Image flow of steel surface defect segmentation

Calculate the mean and standard deviation of the gray boundaries of each region to determit'se gray boundaries of the image. If $WAVG_K(y) < MaxOG \cup WAVG_K(y) > MixOG$, it is set to an effective block, the set value is updated to $MaxOG$ and $MixOG$, and the upper and determine the

lower boundary of image gray levels. Otherwise, its set to an invalid block, the calculation formula is as follows:

$$BGUB = min\left(254, WAVG_K(y) + 2^*WSDV_K(y)\right) \quad (7)$$

$$BGDB = WAVG_K(y) - 2^*WSDV_K(y) \quad (8)$$

$WAVG_K(y)$ is the gray mean value, $WSDV_K(y)$ is the gray standard deviation, K is the block number, and OG is the gray effective value. $Image\ point > BGDB \cup Image\ point < BGUB$, it is determined as a defective image of the strip surface, the normal region and defect boundary region of the steel surface image are extracted, and then the singular target boundary is determined.

The average gray level $BAVG_K(y)$ and standard deviation of gray level $BSDV_K(y)$ of strip steel are calculated and analyzed. If $BAVG_K(y) + 3^*BSDV_K(y) < 255 \cup BAVG_K(y) - 3^*BSDV_K(y) > 0$, the singular target boundary of high and low light is determined for the effective block, and the calculation formula is as follows:

$$HLB = min\left(254, BAVG_K(y) + 4^*BSDV_K(y)\right) \quad (9)$$

$$LLB = max\left(254, BAVG_K(y) - 4^*BSDV_K(y)\right) \quad (10)$$

$BSDV_K(y)$、$BAVG_K(y)$ are the standard deviation and average value of gray cale in the image. When $image\ point > HLB \cup image\ point < LLB$ is determined to be a singular point, the singular density is set to the gray value of each pixel in the singular point image processed by Gaussian mean. When singular threshold < singular density, the defective pixel is obtained, the connected image of the defective pixel is segmented from the original image, and then the edge segmentation image is carried out. The information image is the defect bitmap and related color level image, which will be used in the subsequent classification.

The enhanced MSR-processed image was segmented, with Fig. 5(a) and (b) displaying the edge segmentation results of the scratch and inclusion from Fig. 2. The results demonstrate complete target segmentation with clearly defined, high-contrast edges, effectively removing background interference.

(a) Scratch enhanced segmentation (b) Inclusion enhancement segmentation
Fig. 5. Segmentation results of defect enhancement images

C. Defect image combination feature extraction

The defective image is segmented from the suspected defect area image, and the important feature information of the classification defect is extracted. For many images that feature information, the texture feature is crucial. The gray co-occurrence matrix [30] is a statistical texture analysis method. This approach quantifies texture characteristics by analyzing spatial relationships between adjacent pixels in digital images. The gray co-occurrence matrix generates high-dimensional data, which is rarely employed directly for texture classification, but is used to describe the texture classification features of defects through the constructed partial quadratic statistics. The local gray correlation quantifies Cor the statistical dependence between the gray level of a pixel and the gray levels of its neighboring pixels.

$$Cor = \sum_{i=0}^{L-1}\sum_{j=0}^{L-1}\frac{i\times j\times P(i,j)-\mu_x\mu_y}{\sigma_x\sigma_y} \quad (11)$$

$P(i,j)$ is the gray co-occurrence matrix, μ_x, μ_y is the horizontal row mean and column mean row standard deviation of the co-occurrence matrix, σ_x, σ_y is the row standard deviation and column standard deviation respectively.

The contrast of image sharpness and texture groove depth is calculated as follows:

$$Var^2 = \sum_{i=0}^{L-1}\sum_{j=0}^{L-1}\left(i-\bar{j}\right)^2 P(i,j) \quad (12)$$

The textural energy metrics and the energy of gray level distribution uniformity:

$$E = \sum_{i=0}^{L-1}\sum_{j=0}^{L-1}P(i,j)^2 \quad (13)$$

Entropy is a measure of image information. Texture analysis frequently involves quantifying how random or ordered the pixel intensities are within a region, the formula is as follows:

$$s = -\sum_{i=0}^{L-1}\sum_{j=0}^{L-1}P(i,j)log\,P(i,j) \quad (14)$$

The uniformity of image texture, the Idm measuring the degree of local change of image texture and the formula is as follows:

$$D = \sum_{i=0}^{L-1}\sum_{j=0}^{L-1}\frac{P(i,j)}{1+(i-j)^2} \quad (15)$$

The principle of maximum entropy threshold segmentation [31] was adopted to extract the features of the defect target area ratio and aspect ratio. The ratio of the number of pixels in the target area to the image area is used as the area ratio, and the formula is as follows:

$$R = \frac{A_O}{A} \quad (16)$$

A_O is the defect area, A is the image area. The boundary of the partitioned defect target area is marked by the minimum external rectangle of the defect area. The aspect ratio of the rectangular box is calculated as follows:

$$r = \frac{l}{w} \quad (17)$$

l is the length, w is the width. Through the statistics of the defect boundary information on the number of pixels to get roundness, the roundness ratio calculation formula is as follows:

$$e = \frac{4\pi A_O}{C^2} \quad (18)$$

C represents the circumference of the defect. When $e = 1$, it assumes a perfectly circular configuration. As the eccentricity parameter e decreases, the resultant morphology becomes progressively more irregular, accompanied by a corresponding increase in the deviation from the idealized form. Texture features Co, Et and Idm are used and shape features Ar, As and Ro of defects are extracted as discriminant features for classification. The combined features extracted are input into the model, and the corresponding classification results are output. Combined feature extraction provides effective support for defect classification.

III. Strip Steel Defect Image Classification Based on LPSO-PNN

A. LPSO algorithm

The PSO algorithm [32], functioning as a population-driven stochastic search mechanism. A single

population has N particles and searches randomly in 3D space. The optimal solution is sought through continuous iteration. The update method of particle position is as follows:

$$\begin{cases} v_{id}^{t+1} = w \times v_{id}^{t} + c_1 \times r_1 \times (ipbest_{id} - x_{id}^{t}) \\ \qquad\qquad + c_2 \times r_2 \times (gpbest_{id} - x_{id}^{t}) \\ x_{id}^{t+1} = x_{id}^{t} + v_{id}^{t+1} \end{cases} \quad (19)$$

w is the inertia weight coefficient, c_1、c_2 is the learning factor, r_1、r_2 obtains randomly from the interval (0,1) a number obeying a uniform distribution, $ipbest_{id}$ is the historical best position searched by a single particle, and $gpbest_{id}$ is the historical best position searched by the particle population.

Because the traditional PSO algorithm was prone to local optimization and low population richness, this study adopts the nonlinear decreasing inertia weight coefficient to update the particle swarm to avoid getting stuck in a locally optimal solution. Meanwhile, the Logistic chaotic map is used to optimize the initial state of the population particles, which strengthens the global particle traversal optimization ability.

1) Inertial weight coefficient of nonlinear decline

The PSO algorithm uses an adaptive inertia weight that decreases nonlinearly over iterations to balance global exploration and local optimization, which is calculated as follows:

$$w(m) = w_{ini}(w_{ini} - w_{fin})ln(M - m)/lnM \quad (20)$$

w_{ini}, w_{fin} are the initial inertia weight coefficients and final weight coefficients at the time of iteration, respectively. M, m denote the maximum and current number of iterations, respectively.

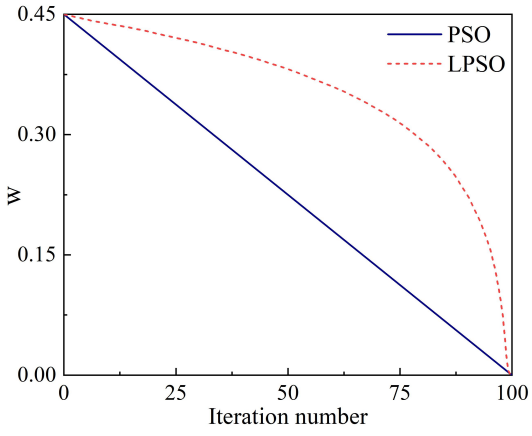

Fig. 6. Decline curve of inertia weight coefficient

Fig. 6 presents a comparative analysis of the inertia weight factor decay curves between the PSO and LPSO algorithms, revealing distinct differences in their weight adjustment mechanisms. The PSO algorithm tends to fall into the local optimum in the first 100 iterations when the algorithm decreases linearly, while the LPSO algorithm, on the other hand, increases the solution precision with the same iteration count by introducing a local search factor. The LPSO algorithm has a stronger global search capability and more stable convergence characteristics, mainly due to its dynamic adjustment mechanism. The LPSO algorithm has stronger overall search capability and more stable convergence characteristics, which is mainly due to its dynamically adjusted weight decay mechanism. The consequences confirm that the LPSO algorithm is preferable in terms of convergence accuracy and robustness compared to the conventional PSO.

2) Logistic chaotic map

The chaotic map based on one-dimensional Logistic equation is as follows:

$$R_{n+1} = \mu R_n (1 - R_n) \quad (21)$$

R_n, R_{n+1} is the chaotic sequence, $R_n \in [0,1]$, μ is the control parameter, generally $\mu \in [3.56,4]$, when μ closer to 4, the more intense the chaotic state.

Equations (20) and (21) are substituted into equation (19) to obtain the particle position update equation of the LPSO algorithm:

$$\begin{cases} v_{id}^{t+1} = w(m) \times v_{id}^{t} + c_1 \times R_1 \times (ipbest_{id} - x_{id}^{t}) \\ \qquad\qquad + c_2 \times R_2 \times (gpbest_{id} - x_{id}^{t}) \\ x_{id}^{t+1} = x_{id}^{t} + v_{id}^{t+1} \end{cases} \quad (22)$$

The distance D_{id} between the optimal particle position and the origin is calculated, and the reciprocal of the distance is used as the determination value S_{id} of the optimal particle position:

$$\begin{cases} D_{id} = \sqrt{x_{id}^{t+1\,2}} \\ S_{id} = \frac{1}{D_{id}} \end{cases} \quad (23)$$

In the process of global particle traversal optimization, it goes through many iterations. When the iteration limit is reached, the optimal particle position is updated, and the corresponding optimal particle position S_{id} is the optimal smoothing factor σ of PNN.

B. Strip steel defect image classification based on LPSO-PNN

In the face of complex classification problems, the PNN network is fast to train and can guarantee the optimal solution under the Bayesian decision criterion. In this study, we employ PNN for the analysis and classification of steel surface defect datasets, which are divided into four layers: the input layer, hidden layer, summation layer, and output layer. Its structure is shown in Fig. 7.

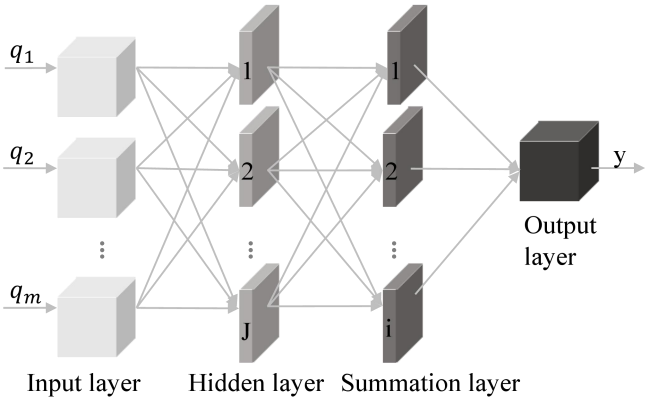

Fig. 7. PNN structure diagram

J is the number of neurons in the hidden layer, i is the number of training sample categories, and y is the output layer. The extracted combined characteristics are input into the model as training samples. The relationship between each mode of the training sample and the input layer is as follows:

$$\Phi(q) = \frac{1}{(2\pi)^{\frac{d}{2}}\sigma^d}\frac{1}{m}exp\left(-\frac{(X-X_i)(X-X_i)^T}{2\sigma^2}\right) \quad (24)$$

d is the dimension of the space where the vector to be classified resides, m is the number of defective training samples, X_i is the ith training vector of the defect, and σ is the smoothing factor of the probability density function.

In the traditional PNN network, the same smoothing factor σ is selected for all parameters. When the smoothing factor takes a single value, the influence of different samples on the correct classification results cannot be correctly reflected. Therefore, different σ should be selected for different samples, and the selection of appropriate smoothing factor parameters is the key to determining the classification performance of PNN.

The strip surface flaw detection process based on a modified particle swarm optimization method and a probabilistic neural network is presented in Fig. 8. The specific steps are listed below:

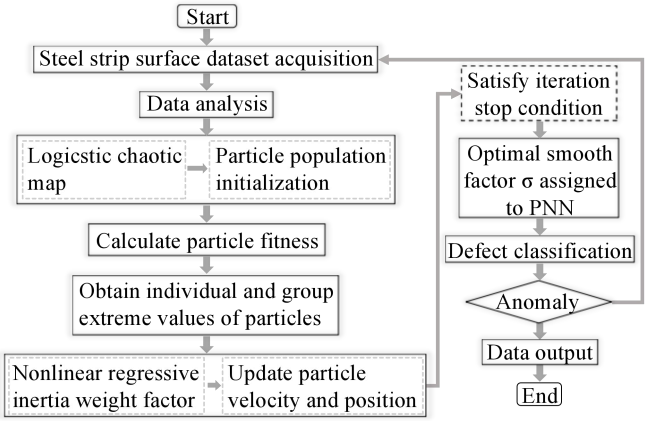

Fig. 8. Strip steel surface defect classification process based on LPSO-PNN

Step 1： 600 images enhanced by improved MSR were selected as training samples, the ratio of training dataset to test dataset is 7:3. The test samples contained 40 defect instances per category, with six extracted features (Co, En, Idm, Ar, As, Ro) being fed into the model.

Step 2： The initial population number was set to 100, the Logistic chaotic map was used to initialize the particle swarm, the chaos control parameter was set to 3.99, the spatial dimension of the particle swarm was set to 1, the number of iterations was set to 80, and the inertial weight coefficient decreased according to equation (20), $w_{ini} = 0.9$、$w_{fin} = 0.4$、$c_1 = 0.5$、$c_2 = 0.5$. The fit values of each particle are calculated, and the individual and population extreme values of each particle are obtained.

Step 3： The velocity and position of the particle are updated by formula (22), and the smoothing factor, σ is obtained after the iteration condition is satisfied. Otherwise, return to step 2.

Step 4： The optimal smoothing factor, σ is assigned to the PNN algorithm, and the combined features of steel surface defect images are classified through the four-layer network. The statistical classification accuracy is averaged, and the defect types are output.

IV. Experimental Results and Analysis

A. Verify the validity of selected combined features

Multiple array CCD cameras and light sources were set up above the experimental table's steel plate, and the light source's angle was adjusted. The camera scan is triggered by the code disk signal of the steel running synchronously in the field automation network. Based on the target steel lighting effect analysis and adaptive control method, the light intensity control is realized to adapt to the complex texture changes of the on-site steel. 6480 enhanced images were selected as the experimental data, 1620 as the training set, and 950 as the test set. Table 1 presents the computed mean values of Co, En, and Idm features across four spatial orientations.

TABLE I
Characteristic Mean Value for Surface Defect Detection of Steel Plate

Feature average	Cr	In	Pa	Sc	Ps
Contrast	13.0831	16.9335	7.5262	46.7881	3.8013
Entropy Inverse	5.6857	6.0320	5.4595	6.2813	5.2804
Different moment	0.4088	0.3183	0.4876	0.2389	0.5543

Cr = scratches, In = inclusion, Pa = patches; Sc = scab, Ps = pitted surfaces

The highest contrast is Sc and the lowest is Ps, with Sc being 12.3 times more varied than Ps. This is because Sc has a large defect area and its local gray scale variation is the most significant, while Ps is the most uniform. The highest value of entropy is 6.2813, and the lowest value is 5.2804, which is a small difference. This is because Sc has the highest complexity of defect information, and Ps is the most homogeneous. The highest value of the inverse difference moment is 0.5543, and the lowest value is 0.2389, with a negative correlation between high contrast and low Sc difference moments, because Ps has the most homogeneous texture and Sc has the most heterogeneous texture.

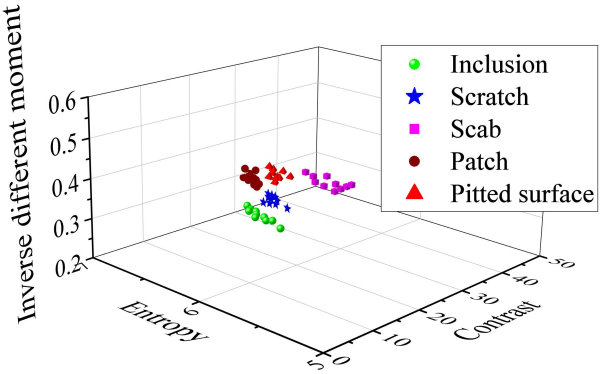

Fig. 9. 3D feature distribution of strip steel plate defects

Fig. 9 visualizes the 3D distribution of three key texture descriptors Co, En, and IDM, where scatter plots demonstrate clear separation across all five defect categories. The extraction results of shape features of images with different defects are systematically presented in Table 2.

TABLE II
Shape Feature Extracted Outcome of Surface Defect Type

Shape feature	Cr	In	Pa	Sc	Pc
Area ratio	3.1	8.48	50.89	23.83	1.70
Aspect ratio	14.47	5.24	1.36	1.91	1.21
Roundness	0.42	0.46	0.75	0.78	0.87

When an image with multiple defective regions is present, the ratio of the sum of the areas of the multiple defective regions to the areas of the image is used as the desired area ratio. The As and Ro of the largest defects are the same as those shown in the image. Finally, these six discriminative

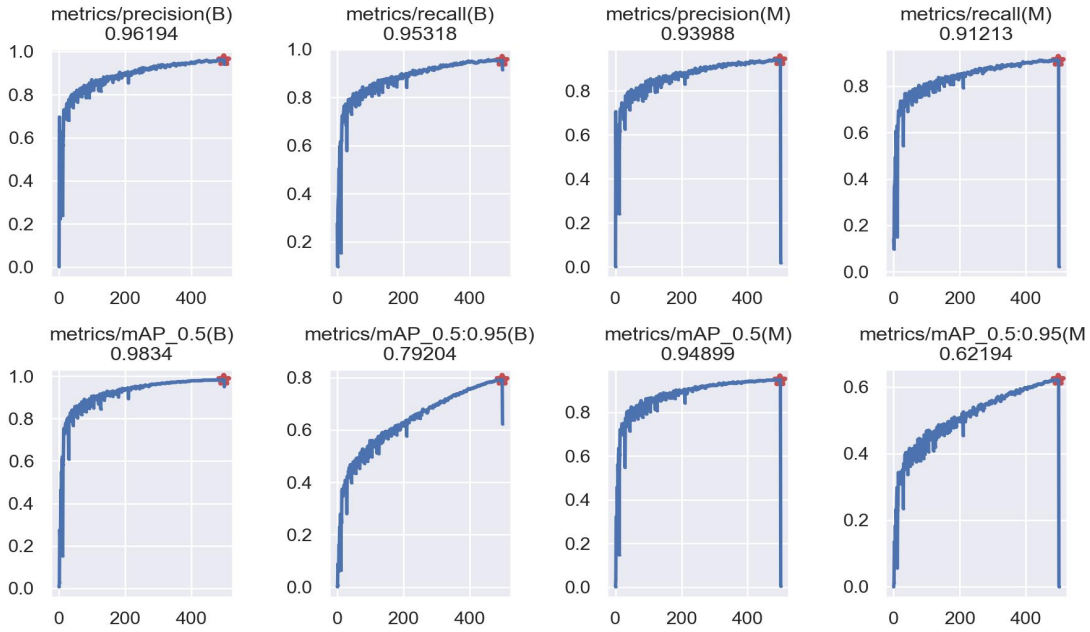

Fig. 10. LPSO-PNN evaluation index curve

features, Co, En, IDM, AR, AS, and Ro, constitute the final feature vector for defect classification.

Pa and Sc have much higher area ratios than other defects, while Ps and Cr are the lowest. This is because Pa and Sc may be large-sized defects while Ps and Cr are small-sized defects. It is in the middle and may have medium-sized defects. Cr is extremely high with 14.47. Roundness gradually increases from Cr to Ps, indicating that the shape of the defects is gradually approaching perfect roundness from irregular. Ps may be nearly round holes, and Cr is highly irregular in shape. The aspect ratios indicate an extremely elongated shape. In is next highest at 5.24, while Pa, Sc, and Ps all have aspect ratios close to 1, indicating that Cr and In are cracked or linear defects, Pa, Sc, and Ps are holes or massive defects.

B. Comparative experimental analysis

To verify the proposed algorithm's classification effect, we used precision, recall, accuracy, and test time as metrics. The identification precision is calculated by inputting the same parameters in the comparison model. The proposed algorithm was compared with the current popular classification model, and the steel surface defects were tested.

Fig. 10 illustrates the accuracy and recall curves of defect detection under different confidence thresholds. Both metrics consistently improve as the number of training iterations increases. After 400 rounds of training, the system's precision for detecting boxes and masks was 0.96194 and 0.93988, with recalls of 0.95318 and 0.91213, respectively. When the mean Average Precision (mAP) threshold was set at 0.5, the system achieves box recognition accuracy of 0.9834. However, when evaluated under the stricter mAP@0.5:0.95 metric, the accuracy drops to 0.79204, likely due to insufficient training iterations. When the number of training rounds is lower than 500, the mAP is set to 0.5, and the system is good at detecting surface defects on the strip. When the training reaches more than 1,000 rounds, the mAP is in the range of 0.5:0.95, and the accuracy will be above 0.95. Furthermore, detection accuracy continues to improve with additional training, confirming the high stability and robustness of the proposed method.

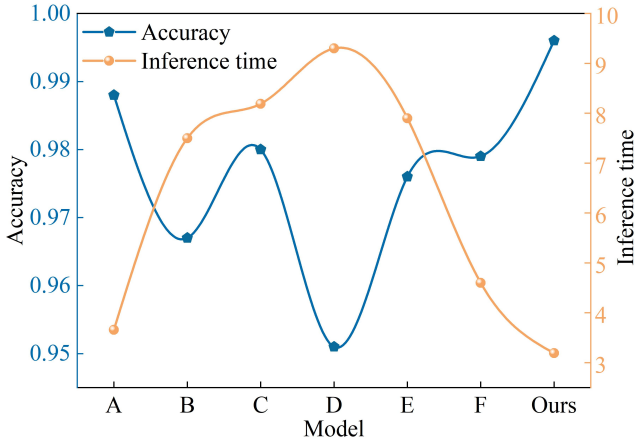

Fig. 11. Accuracy and test time of the seven models

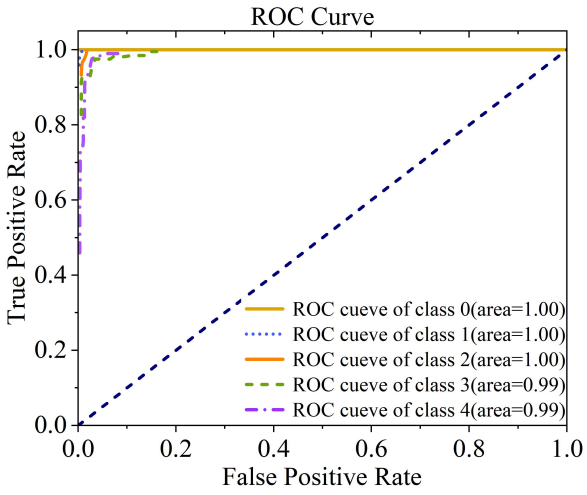

Fig. 12. ROC curve

To compare the effectiveness of the model proposed in this study, five popular models, MobileNetv (A), ShuffleNetv (B), DenseNet (C), ShuffleNetv (D), and CNN (E) are listed for comparison.

By observing Fig. 11, the accuracy rate of the LPSO-PNN model is 99.57%, the detection time is 3.19s, the classification accuracy is the highest, the test time is the shortest, which is 1% higher than that of model A, and the test

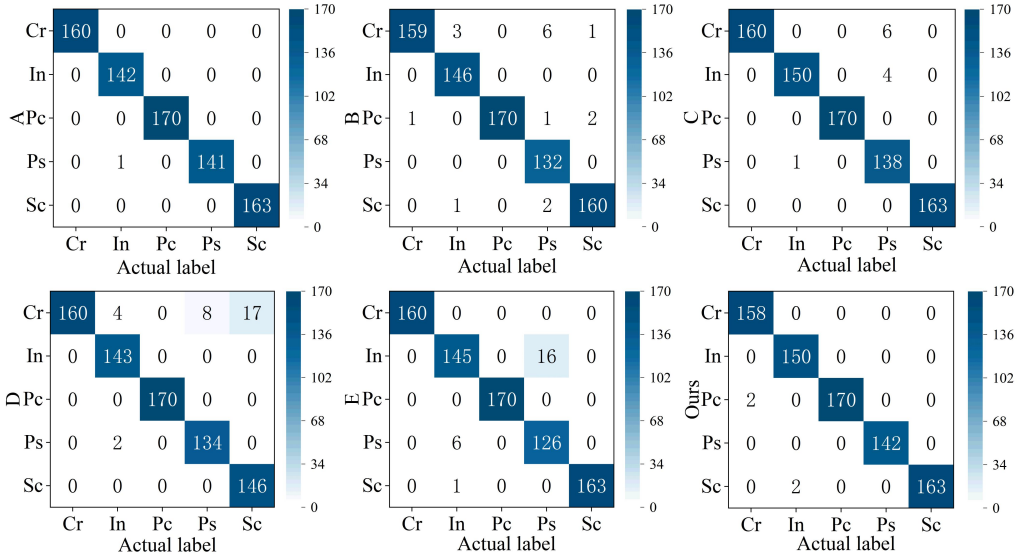

Fig. 13. Confusion matrix of classification model

time is 0.47s shorter. This study compared with the F model, the accuracy rate increased by 1.7% in a short time of 1.4 s, more than other algorithms. The LPSO-PNN model achieves high classification accuracy with reduced computational latency in strip steel surface defect detection, demonstrating enhanced compatibility with industrial real-time inspection requirements. Meanwhile, the receiver operating characteristic (ROC) curve provides a quantitative evaluation of classification model performance, with the area under the curve (AUC) serving as a key discriminative metric where higher values indicate superior class separation capability. Fig. 12. depicts the ROC curve of the LPSO-PNN model. The LPSO-PNN model exhibits perfect classification performance AUC=1.00 for Ps, Pa, and Sc, while maintaining near-ideal discriminative power AUC=0.99 for In and Cr, thereby validating its industrial-grade detection precision in steel surface quality control.

A multi-class confusion matrix was implemented to evaluate the LPSO-PNN model's diagnostic accuracy across five steel surface defect categories, enabling granular analysis of inter-class misclassification patterns. Fig. 13. provides a comparative visualization of classification accuracy across competing methodologies. The vertical coordinate denotes the true category, the horizontal coordinate denotes the predicted category. The confusion matrix showed that the LPSO-PNN model had the best classification performance.

The confusion matrix combines the accuracy of recognition of defect types as well as misclassification. Since Cr defects are primarily concentrated in a single orientation while Sc defects are distributed in all directions, these two categories exhibit certain similarities. This makes Cr defects in specific orientations particularly prone to being misclassified as Sc defects during recognition. The LPSO-PNN effectively addresses this issue of inter-class confusion between defect types. As shown in Fig. 13, the proposed method achieves significantly higher recognition accuracy for In defects compared to both Model A and Model F. The Ps and In classification accuracies of both D and E models are not satisfactory, and the present model improves this significantly as well. LPSO-PNN is significantly better than models B and C in identifying Ps defects. In conclusion, the proposed model can maintain a high defect recognition efficiency under complex conditions and short inference time.

V. Conclusion

This paper studies strip steel surface defects. Similar image characteristics, complex shapes, and so on are proposed based on the combination of feature extraction and probabilistic neural network method for hot rolling strip steel surface defect detection and recognition.

1) Image enhancement was performed on the acquired steel defect dataset, and the proportion of calculated information entropy was used to automatically determine the weights of different scales. The adaptive threshold selects the enhanced image, and the suspected defects are located by the singular point density analysis method. The image segmentation of the defect area is completed. The enhancement of a defective image is clearer than the original image, and the image quality of the segmentation effect is better.
2) A quadratic statistic and maximum entropy threshold segmentation method were constructed to extract the texture and shape features of defects, and the combined features were used as the discriminant parameters of the LPSO-PNN classification model. The verification shows that the combined feature makes the scatter points of the five defects have no intersection, and achieves a good separation effect, reflecting the combined feature's effectiveness.
3) The Logistic chaotic map and a nonlinear decreasing inertia weight coefficient are used to update the particle swarm, which is used to select the optimal smoothing factor of PNN. LPSO-PNN is assigned to PNN to classify the surface defects of steel. Compared with other methods, the practicability and effectiveness of the LPSO algorithm in optimizing PNN for defect classification are verified.

In our future work, we will investigate more defect types and identification methods to enhance the architecture and intelligent monitoring performance of the monitoring architecture.

REFERENCES

[1] C. Zhao, X. Shu, X. Yan, X. Zuo, F. Zhu, "RDD-Yolo: A modified Yolo for detection of steel surface defects," *Measurement*, vol. 214, p. 112776, 2023.

[2] S. Gao, M. Chu, L. Zhang, "A detection network for small defects of steel surface based on YOLOv7," *Digital Signal Processing*, vol. 149, p. 104484, 2024.

[3] P. M. Bhatt, R. K. Malhan, P. Rajendran, B. C. Shah, S Thakar, Y. J. Yoon, and S. K. Gupta, "Image-based surface defect detection using deep learning: A review," *Journal of Computing and Information Science in Engineering*, vol. 21, no. 4, pp. 1-23, 2021.

[4] M. Li, H. Wang, Z. Wan, "Surface defect detection of steel strips based on improved YOLOv4," *Computers and Electrical Engineering*, vol. 102, p. 108208, 2022.

[5] M. X. Chu, Z. X. Zhai, L. M. Liu, and G. H. Liu, "Steel plate surface defects classification method using multiple hyper-planes twin support vector machine with additional information," *Engineering Letters*, vol. 31, no. 3, pp. 1016-1024, 2023.

[6] Y. C. Zhang, Z. C. Huang, Y. Q. Jiang, and Y. L. Jia, "Mechanical properties of B1500HS/AA5052 joints by self-piercing riveting," *Metals*, vol. 13, no. 2, p. 328, 2023.

[7] X. Sun, J. Gu, S. Tang, and J. Li, "Research progress of visual inspection technology of steel products—a review," *Applied Sciences*, vol. 8, no. 11, p. 2195, 2018.

[8] K. Lu, W. Wang, X. Feng, Y. Zhou, Z. Chen, Y. Zhao, and B. Wang, "Surface defects identification of hot rolled strip based on lightweight convolutional neural network," *ISIJ International*, vol. 63, no. 12, pp. 2010-2016, 2023.

[9] H. Yang, Y. Wang, J. Hu, J. He, Z. Yao, and Q. Bi, "Deep learning and machine vision-based inspection of rail surface defects," *IEEE Transactions on Instrumentation and Measurement*, vol. 71, no. 24, pp. 1-14, 2021.

[10] L. Li, W. H. Peng, Z. P. Duan, and S. S. Pu, "Adaptive illumination estimation for low-light image enhancement," *Engineering Letters*, vol. 32, no. 3, pp. 531-540, 2024.

[11] Y. Qi, Z. Yang, W. Sun, M. Lou, J. Lian, W. Zhao, X. Deng, and Y. Ma, "A comprehensive overview of image enhancement techniques," *Archives of Computational Methods in Engineering*, vol. 29, no. 23, pp. 583-607, 2021.

[12] B. K. Chakraborty, M. K. Bhuyan, "Image specific discriminative feature extraction for skin segmentation," *Multimedia Tools and Applications*, vol. 79, no. 27, pp. 18981-19004, 2020.

[13] F. Bardozzo, B. De La Osa, and Ľ. Horanská, "Sugeno integral generalization applied to improve adaptive image binarization," *Information Fusion*, vol. 68, no. 1, pp. 37-45, 2021.

[14] T. R. Singh, S. Roy, O. I. Singh, T. Sinam, and K. M. Singh, "A new local adaptive thresholding technique in binarization," *Arxiv preprint arxiv*, vol. 8, no. 6, pp. 271-277, 2012.

[15] M. T. N. Truong, S. Kim, "Automatic image thresholding using Otsu's method and entropy weighting scheme for surface defect detection," *Soft Computing*, vol. 22, pp. 4197-4203, 2018.

[16] V. Akhil, G. Raghav, N. Arunachalam, and D. S. Srinivas, "Image data-based surface texture characterization and prediction using machine learning approaches for additive manufacturing," *Journal of Computing and Information Science in Engineering*, vol. 20, no. 2, p. 021010, 2020.

[17] W. Sun, N. Zeng, and Y. He, "Morphological arrhythmia automated diagnosis method using gray-level co-occurrence matrix enhanced convolutional neural network," *IEEE Access*, vol. 7, pp. 67123-67129, 2019.

[18] L. Chu, B. Liu, L. Xu, Z. W. Li, and B. F. Zhang, "Speckle quality evaluation based on gray level co-occurrence matrix," Laser Optoelec*tron. Progress*, vol. 58, pp. 235-243, 2021.

[19] W. Jie, C. Manlong, L. Kui, D. Min, and W. Kun, "Prickly ash image recognition based on HSV and shape feature fusion," *Journal of Chinese Agricultural Mechanization*, vol. 42, no. 10, p. 180, 2021.

[20] H. Wang, X. Jin, T. Zhang, and J. Wang, "Convolutional neural network-based recognition method for volleyball movements," *Heliyon*, vol. 9, no. 8, p. 18124, 2023.

[21] J. An, M. D. Putro, A. Priadana, and K. H. Jo, "Improved YOLOv5 network with CBAM for object detection vision drone," *IEEE International Conference on Industrial Technology*, pp. 1-6, 2023.

[22] H. Jiang, Z. Diao, T. Shi, Y. Zhou, F. Wang, W. Hu, X. Zhu, S. Luo, T. Gong, and Y. D. Yao, "A review of deep learning-based multiple lesion recognition from medical images: classification, detection and segmentation," *Computers in Biology and Medicine*, vol. 157, p. 106726, 2023.

[23] B. Liu, X. Zhang, X. Zou, J. Cao, and Z. Peng, "Biological tissue damage monitoring method based on IMWPE and PNN during HIFU treatment," *Information*, vol. 12, no. 10, p. 404, 2021.

[24] Q. Tan, X. Mu, M. Fu, H. Yuan, J. Sun, G. Liang, and L. Sun, "A new sensor fault diagnosis method for gas leakage monitoring based on the naive Bayes and probabilistic neural network classifier," *Measurement*, vol. 194, no. 15, p. 111037, 2022.

[25] S. Gao, Q. Wang, Y. Zhang, "Rolling bearing fault diagnosis based on CEEMDAN and refined composite multiscale fuzzy entropy," *IEEE Transactions on Instrumentation and Measurement*, vol. 70, pp. 1-8, 2021.

[26] W. Di, M. Wang, X. Sun, F. Kang, H. Zheng, and J. Bian, "Identification of rock bolt quality based on improved probabilistic neural network," *International Journal of Modelling*, vol. 30, no. 2, pp. 105-117, 2018.

[27] X. B. Huang, L. Yang, Y. Zhang, W. Cao, and L. C. Li, "Image enhancement-based detection method of nonsoluble deposit density levels of porcelain insulators," *Autom Electr Power Syst*, vol. 42, no. 14, pp. 151-157, 2018.

[28] Y. Y. Zhang, "Research of haze color image enhancement based on multiscale Retinex," *Packag J*, vol. 8, pp. 60-65, 2016.

[29] X. Yang, J. Hu, L. Wu, L. Xu, W. Lyu, C. Yang, and W. Zhang, "Binary ghost imaging based on the fuzzy integral method," *Applied Sciences*, vol. 11, no. 13, p. 6162, 2021.

[30] S. Aouat, I. Ait-hammi, I. Hamouchene, "A new approach for texture segmentation based on the Gray Level Co-occurrence Matrix," *Multimedia Tools and Applications*, vol. 80, no. 16, pp. 24027-24052, 2021.

[31] Z. Li, L. Chen, B. Zhang, H. Shi, and T. Long, "SAR image oil spill detection based on maximum entropy threshold segmentation," *Signal Process*, vol. 35, pp. 1111-1117, 2019.

[32] M. A. E Mohamed, A. M. Mahmoud, E. M. M. Saied, and H. A. Hadi, "Hybrid cheetah particle swarm optimization based on optimal hierarchical control of multiple microgrids," *Scientific Reports*, vol. 14, no. 1, p. 9313, 2024.